

**Experimental and computational study of the influence of pre-damage patterns in unreinforced masonry crack propagation due to induced, repeated earthquakes**

Korswagen Eguren, Paul; Longo, Michele; Meulman, Edwin; Rots, Jan

**Publication date**

2019

**Document Version**

Accepted author manuscript

**Published in**

Proceedings of the Thirteenth North American Masonry Conference

**Citation (APA)**

Korswagen Eguren, P., Longo, M., Meulman, E., & Rots, J. (2019). Experimental and computational study of the influence of pre-damage patterns in unreinforced masonry crack propagation due to induced, repeated earthquakes. In P. B. Dillon, & F. S. Fonseca (Eds.), *Proceedings of the Thirteenth North American Masonry Conference : June 16-19, 2019, Salt Lake City, UT, USA* (pp. 1628-1645). TMS.

**Important note**

To cite this publication, please use the final published version (if applicable). Please check the document version above.

**Copyright**

Other than for strictly personal use, it is not permitted to download, forward or distribute the text or part of it, without the consent of the author(s) and/or copyright holder(s), unless the work is under an open content license such as Creative Commons.

**Takedown policy**

Please contact us and provide details if you believe this document breaches copyrights. We will remove access to the work immediately and investigate your claim.

<b>Manuscript title:</b>	Experimental and computational study of the influence of pre-damage patterns in unreinforced masonry crack propagation due to induced, repeated earthquakes
<b>Author 1 name:</b>	Paul A. Korswagen
<b>Author 2 name:</b>	Michele Longo
<b>Author 3 name:</b>	Edwin Meulman
<b>Author 4 name:</b>	Jan G. Rots
<b>Author 5 name:</b>	
<b>Author 6 name:</b>	
<b>Author 7 name:</b>	
<b>Author 8 name:</b>	
<b>Author 9 name:</b>	
<b>Abstract:</b> (300-word limit)	<p>Induced seismicity in the north of the Netherlands has recently exposed unprepared, unreinforced masonry structures to considerable earthquake risk. While the ultimate-limit state capacity of the structures is vital to assess the individual's risk, their behaviour during more frequent, lighter earthquakes, leading to 'lighter damage', has shown to be strongly linked to economical losses and societal unrest. When observing the light damage caused by minor earthquakes, the existing state of the structure appears to be highly relevant for the final damage intensity and configuration: earthquakes that may have otherwise caused no apparent damage, may intensify existing damage. In particular, incipient damage due to settlements is common in the baked-clay and calcium-silicate brick masonry structures of the region.</p> <p>This paper details the study of full-scale laboratory walls, pre-damaged following typical (crack) patterns caused by settlements and tested with quasi-static lateral loads. The aggravation of the damage during a relevant number of load cycles is monitored using full-field digital image correlation. The damage is quantified objectively using a purposely-developed damage parameter.</p> <p>The tests are used (together with previous studies) to further calibrate computational finite element models, which coupled with detailed soil-structure interaction boundary conditions, are then employed to assess a larger number of structural geometries and pre-damaged configurations exposed to (repeated) induced earthquake acceleration histories.</p> <p>Both experimental and computational approaches show that settlement pre-damage in masonry structures increases the likelihood and the amount of further damage. This is more easily observed when some initial, yet limited damage exists and the masonry wall is exposed to moderate earthquake vibrations in the order of 30 millimetres per second.</p>
<b>Keywords:</b>	Unreinforced Masonry, Induced Seismicity, Light Damage, Damage Aggravation, Crack Propagation

## **1. INTRODUCTION**

Recent earthquakes in the Groningen region in the north of the Netherlands have caused or contributed to the light damage of some masonry houses (see for instance, NAM, 2016). While high ground vibration levels may lead to severe damage, these are not common and are limited to a small area of impact. Conversely, lighter vibrations, caused by more frequent lighter earthquakes or uncommon, distant larger earthquakes, are related to the lower damages states associated with the cracking of masonry, the most common building material in the region. This damage is usually expressed as fine cracks running on masonry joints, and between structural and non-structural elements.

The research field assessing the ultimate strength and near collapse capacity of structures and their associated risk to human life is now rich and has thus started to shift away from characterising the higher damage states, to implementing strengthening measures and to understanding of light damage. Focus is now given at comprehending the processes that cause limited damage. The reader is referred to Korswagen et al. (2019) for a more complete exploration of the literature in the field.

This light damage, in this context denoted as ‘damage state one’ (DS1) see for example de Vent et al. (2011), has led to economical losses and societal unrest, yet seems to be the most difficult to estimate and quantify. The difficulty arises likely due to the aesthetic nature of the damage, the variability of the structures, and most importantly, the interaction of multiple damage causes. Van Staaldunin et al. (2018) conducted an investigation of the observed damage in the region by thoroughly analysing more than 60 cases. The damage causes were given a likelihood index for each case. Overall, actions due to differential settlements were seen to be the predominant cause of damage. Moreover, exploratory computational models showed that lightly damaged structures expressed increased damage after being subjected to an earthquake time history.

Accordingly, while damage caused by larger earthquakes can be apparent, the damage triggered by lighter earthquakes is not as easy to attribute and is likely to heavily depend on the initial state of the structure. Previous research explored this relationship and determined that indeed, a lightly damaged structure, due to previous earthquakes or uneven settlements (as mentioned, the latter is a common ailment of many masonry structures with shallow foundations, typical of the region), was more likely to suffer additional damage (see Korswagen et al., 2017). In the previous research, this observation was based on extrapolations made with calibrated finite element models. In this paper, the observation is validated also with experimental tests on full-scale masonry walls, and verified further with improved finite element models.

The paper continues in section 2 with a description and motivation of the laboratory tests of pre-damaged masonry walls, of which results are presented in section 3. Next, section 4 compares these walls against previously tested specimens without any form of pre-damage. Then, section 5 presents the calibration of finite element models against the pre-damaged walls, and details the extrapolation to earthquake time history analyses.

## **2. SETUP OF LABORATORY TESTS ON PRE-DAMAGED WALLS**

A single-wythe masonry wall built with baked-clay bricks in a running bond and having an asymmetrical window opening is used as the main case of this study, see figure 1. The specimens are built to match four walls of identical geometry and material previously tested that are used as benchmarks against which comparisons are drawn. An elaboration of the selection of the material and geometry of the walls is provided in Korswagen et al. (2019). Briefly, the combination of brick and mortar were chosen to

replicate material properties of masonry from the period before 1950, this follows a characterisation study performed by Jafari et al. (2019), see also Jafari et al. (2017). A single-wythe wall was selected to reduce the uncertainty and more easily follow cracks in the masonry. Finally, the window was introduced to better observe cracks, which usually propagate from window corners. The asymmetry of the window position allowed for more complex crack patterns, and its dimensions were picked to resemble real cases (see Graziotti et al., 2017).

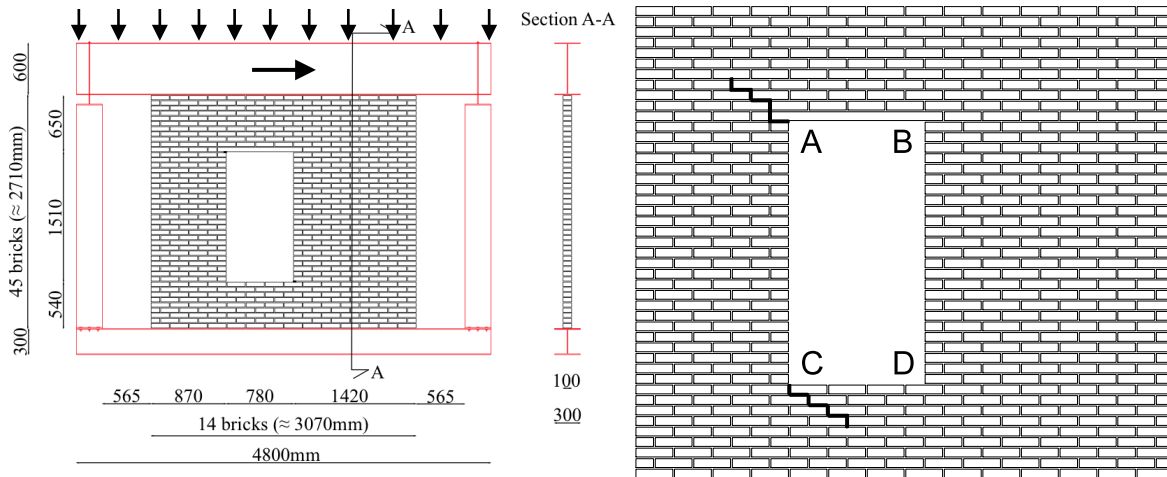


Figure 1. Left, geometry of the masonry wall. Right, position of plastic strips to simulate pre-damage on window corners A and C.

Two identical specimens of the wall described (designated TUD-Comp45 and Comp46, with ‘Comp’ indicating ‘component’) are experimentally tested in this study. The walls are pre-damaged by means of reduced bond at specific joints. The reduction in bond is accomplished by placing strips of PVC at the moment of construction. The strips run along predefined joints simulating the presence of an open crack. The bond between the mortar and the plastic was determined by a series of bond-wrench tests where the bond area between the bricks was reduced by incorporating different ratios of PVC. From these tests, the bond strength of the plastic to the mortar was keyed at around 0% to 5% of the bond between brick and mortar, hence adequately replicating an open crack. The position of the strips is illustrated in Figure 1 and was chosen to mimic uneven settlement damage on the wall, where the right side of the wall settles more than the left. The precise position of ‘cracks’ was determined by a combination of finite element models and review of damage cases, see Figure 2.

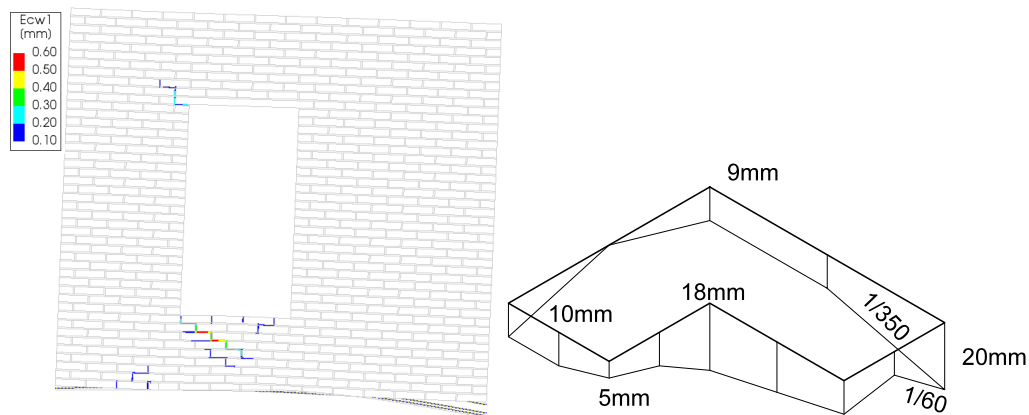


Figure 2. Left, crack width plot of a computational model. Right, example of measurement of bed-joint levelling to determine a settlement configuration which could resemble the employed settlement.

The walls were subjected to an overburden of 0.12MPa during the test, representing a moderate gravity load. The specimens were attached to the testing setup at the bottom and fixed to a top steel beam that was free to rotate but whose horizontal displacement (in the plane of the walls) was prescribed. See Messali et al. (2017) for additional details on the test setup. The walls were then subjected to a step-wise increasing top lateral displacement (drift). The loading protocol consisted of five one-way cyclic steps of 30 cycles each and seven two-way cyclic steps also of 30 cycles each for a total of 360 cycles with a maximum drift of 0.75‰; this is illustrated in Figure 3.

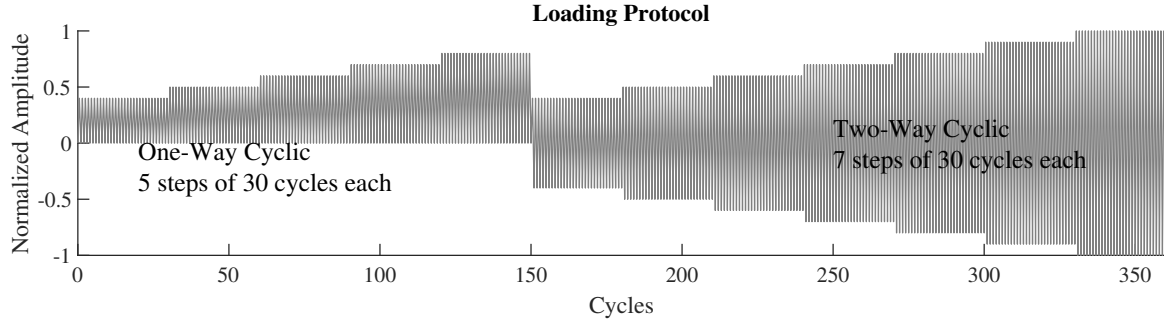


Figure 3. Loading protocol with a high number of small cycles.

The loading protocol was thus the same as employed on the previously tested virgin walls. The number of cycles for each step (30) was chosen to be able to observe a potential damage progression and its stabilisation at the same value of prescribed drift (see here the results of Korswagen et al. 2018). The presence of a one-way portion in the test at the beginning allows for investigation of whether reversal of the loading direction at the crack interfaces influences the progression of damage. The high total number of cycles corresponds to the evaluation of multiple small earthquake excitations and their influence in the accumulation of light damage. Additional reasoning for the loading scheme can be found in Korswagen et al. (2019).

The in-plane displacements of the walls were monitored using digital image correlation (DIC) with a resolution grid of 3x3mm and a precision of 20µm; this allowed for crack monitoring similar to, for example, Didier et al. (2018). This same measuring technique was used on the previously tested walls to successfully monitor crack initiation and propagation. The crack pattern at a given instance during the test was characterised with a damage parameter that determines the damage intensity based on the number, width, and length of the cracks following equation 1. The total of visible cracks is expressed in one number such that the narrowest visible cracks with a width of 0.1mm result in a value of around one ( $\Psi=1$ ), slightly larger cracks of close to 1mm width correspond to two ( $\Psi=2$ ) and cracks of approximately 4mm in width give a value of three ( $\Psi=3$ ). This range corresponds to light damage (DS1). Additional information regarding this parameter can be found in Korswagen et al. (2019).

$$\Psi = 2 \cdot n_c^{0.15} \cdot \hat{c}_w^{0.3} \quad (1a) \quad \hat{c}_w = \sum_{i=1}^{n_c} c_{w,i}^2 \cdot c_{L,i} \cdot \left( \sum_{i=1}^{n_c} c_{w,i} \cdot c_{L,i} \right)^{-1} \quad (1b)$$

Where:

$n_c$  is the number of cracks in the wall/specimen

$\hat{c}_w$  is the width-weighted and length-averaged crack width (in mm) calculated with (1b):

$c_w$  is the maximum crack width along each crack in mm

$c_L$  is the crack length in mm

For  $n_c=1$ ,  $\hat{c}_w = c_w$ . In this expression, the crack width of each crack is measured at their widest point.

### 3. RESULTS OF TESTS OF PRE-DAMAGED WALLS

The behaviour of both pre-damaged walls was partly influenced by the existing crack. While the bottom pre-damaged joints seem to contribute little to the crack development, the weakened joints at the left top corner of the window did influence the crack growth. Especially for the first wall, Comp45, where a full opening and detachment of the left pier was observed with a crack of up to 2mm in width towards the end of the test. See Figure 4c. This also led to reduced hysteresis in comparison to the second wall as evidenced by a more narrow ‘neck’ of the cyclic force-displacement curve presented in Figure 5.

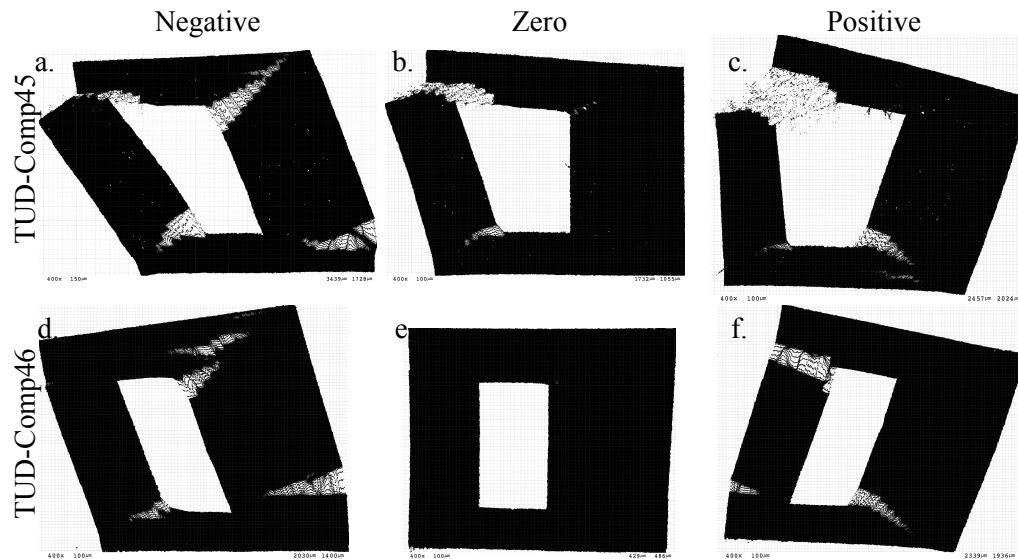


Figure 4. Magnified (400x) deformed shape plots captured using DIC for a negative, zero, and positive drift towards the end of the test (after 300 cycles) for walls Comp45, top, and Comp46, bottom. Note the full detachment of the left pier of Comp45 at this stage.

Here, several noteworthy observations are highlighted. First, even though the walls have a window placed off-centre, the behaviour is similar for the positive and the negative directions; the negative direction, where emphasis is given to the small pier, does show consistently lower strength. Second, the strength degradation due to the repetition of multiple cycles per step, is clearly observable in Figure 5.b and Figure 5.d. On average, the degradation is around 5%. In Figure 5.b, it is also interesting to note how the two-way cyclic portion of the test does not display degradation for the positive drift, but does show it for the negative drift; presumably this is because the one-way cyclic portion of the test has already degraded the wall, but only for the positive drift. Third, the strength during the first step of the two-way cyclic test is significantly lower than it was during the very beginning of the test. This is clear evidence that, even though the wall had only been pushed to approximately 0.65‰ of drift, its behaviour against subsequent excitations has changed.

The degradation per step is also evidenced in the crack progression of the walls throughout the test. Figure 6 shows the crack pattern and the progression of the width of the cracks. Cracks are evaluated from and to a cutoff width of 0.1mm and are required to be longer than 100mm. Here, the increase in crack width of the various cracks does not only occur at the change of step (which is easily identifiable), but also throughout each step. In the case of Comp45, the detachment at the top of the left pier (crack 1) leads to a large crack width and a consequent high value of damage ( $\Psi \approx 3$ ). Here, the large crack increase of crack 1, accompanies propagation of cracks 2 and 4 which are linked to the same failure mechanism (see Figure 4a). In Comp46, the width of the cracks is more uniform, but the steady increase, also within each step, is also present. In both walls, the damage parameter  $\Psi$  also increases steadily.

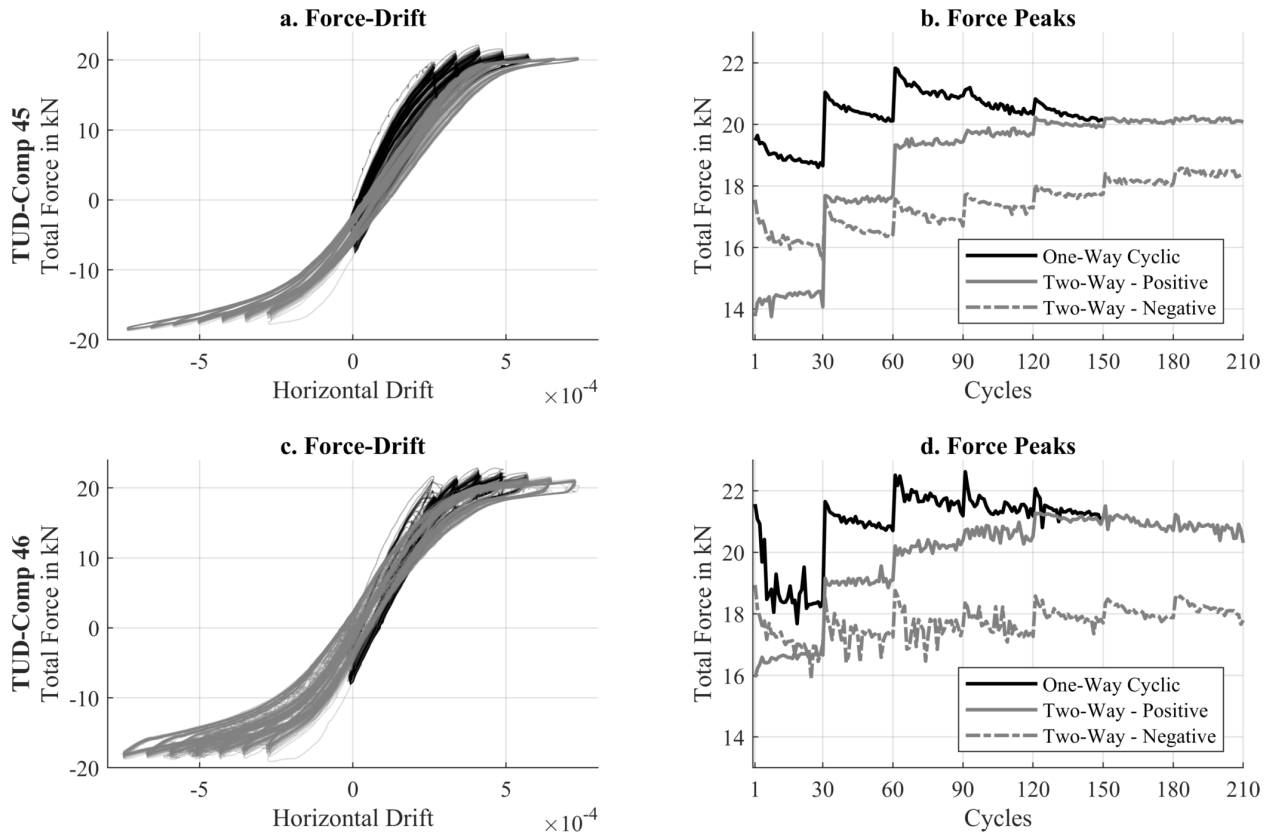


Figure 5. Force-Drift (displacement) plots for pre-damaged walls, including the progression of force peaks during the test. Top, Comp45; bottom, Comp46.

#### 4. COMPARISON AGAINST PREVIOUSLY TESTED NON-DAMAGED WALLS

Four walls without pre-damage have been tested previously (Comp40 to Comp43). When comparing the pre-damaged walls against the walls without pre-damage, one would expect that the non-predamaged walls are stronger. Table 1 shows that this is not the case, all walls case a similar strength. Nevertheless, the stiffness of the pre-damaged walls is noticeably lower than that of the virgin walls, which can be traced to the weakening of the joints. The initial stiffness was determined by dividing a force difference by the corresponding difference of lateral displacement at multiple points during the first loading gradient (see, for instance Figure 5a). Applying the same procedure to multiple loading gradients reveals that, while the initial lateral stiffness achieved values of around 30 kN/mm, the stiffness at the end of the test had decreased by approximately 30%. Similarly, the stiffness decrease of the non-predamaged walls was slightly higher but resulted in similar end values. Since the response of structures to dynamic excitations depends on the stiffness of the structure, damaged structures are thus expected to respond differently.

Table 1. Comparison of lateral stiffness and strength for three virgin and two pre-damaged specimens.

	Initial Lateral Stiffness (kN/mm)				Maximum Base Shear (kN)			
<b>No pre-damage</b>	35.1	38.1	36.9	<b>36.7</b>	21.8	22.1	22.8	<b>22.2</b>
<b>Pre-damaged</b>		27.6	29.3	<b>28.4</b>		21.8	22.6	<b>22.2</b>

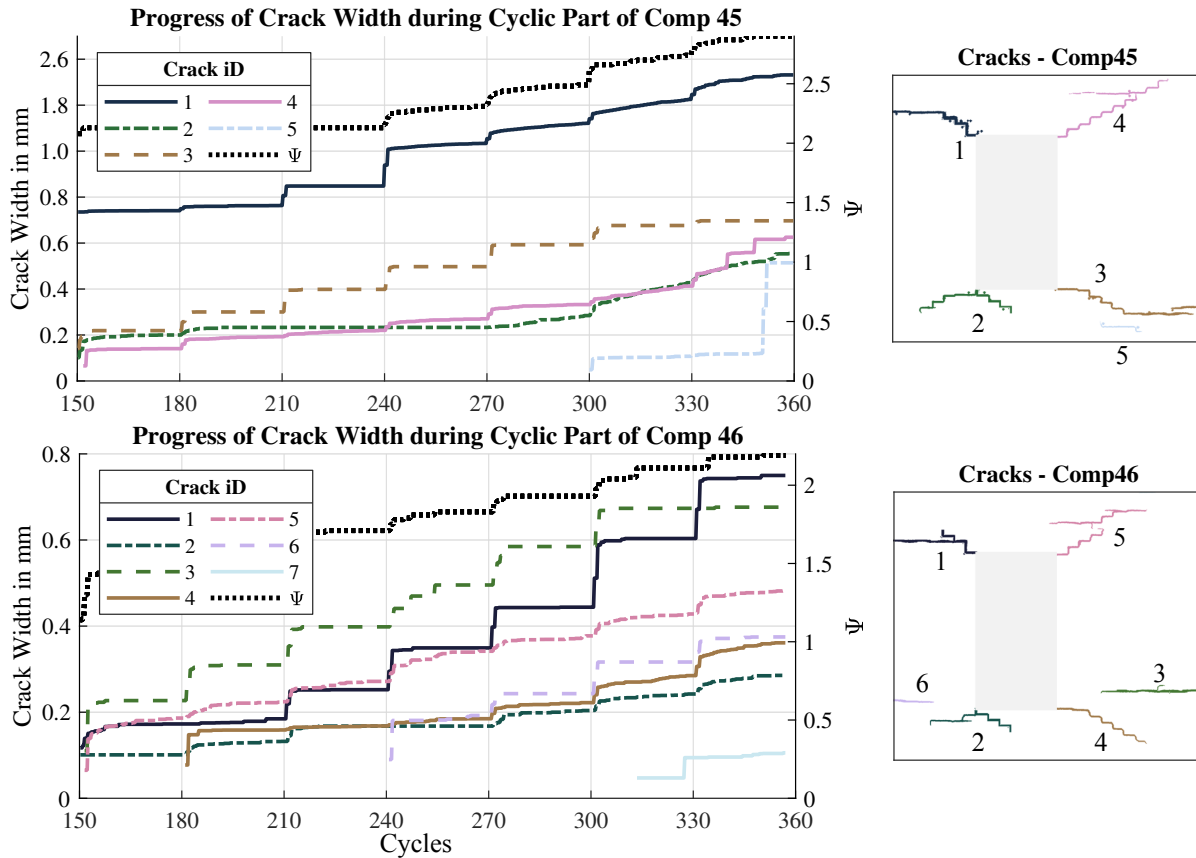


Figure 6. Progression of crack width during two-way cyclic portion of the pre-damaged walls.

When observing the damage parameter  $\Psi$ , a relationship can be traced between the drift to which the walls are exerted to, and their damage intensity. Figure 7 shows that at larger drift values, increased damage is also expected. A power fit is applied to the data outside of the axes (non-zero damage and non-zero drift). For the walls without pre-damage, the curves appear closer to linear fits, while for the walls with pre-damage, the fits have a stronger curvature. Note that the fits do not consider the fact that damage increases at the same value of drift (strength degradation and damage aggravation), and are thus approximate fits. Nonetheless, it would seem that, walls with pre-damage (Comp45 and Comp46) display more severe damage at lower drift values but equalise with the rest of the walls at higher drift values. Note also that pre-damage walls have a significantly higher number of points on the vertical axis, showing detectable damage at zero drift. Additionally, the case of Comp45 where the left pier detached completely from the top of the wall, displays a clear increase in damage in the positive direction. In the negative direction, the damage decreases between 0.4‰ and 0.5‰ before increasing again; this is likely related to the significant amount of sliding occurring at the top of the left pier which closes the crack at the bottom of the left pier, but later contributes to opening it further as depicted in Figure 4a.

The higher damage of Comp45 is also visible in Figure 9, where the width of the four cracks at the window corners is compared for the two-way cyclic portion of the test. In Figure 9a, the crack for Comp45 is significantly wider than the same crack for the other cases. The second pre-damaged wall, Comp46 also shows increased crack-width, evidencing that for the crack at the top left window corner (from here on, crack a), the pre-damage has had an influential effect. This is reasonable, since this crack was partly pre-damaged (see Figure 2), and the failure mechanism related to the in-plane lateral loading fosters the crack propagation over the pre-damaged joints. Conversely, the crack at the bottom left



window corner (crack c, Figure 9c) does not display unusual width; in this case, the pre-damaged joints trigger the presence of a crack but do not seem to affect its propagation as the crack travels in a different direction (see Figure 9). In fact, the cracks at the left corners of the window (a and c) are not part of the same failure mechanism (see Figure 4) but appear to be related when significant sliding occurs at the top of the pier. Comp41 also shows a large crack width at the top of the left pier (a) which is evidence of a full detachment of the pier towards the end of the test; then, the crack width at the bottom of the pier (c) grows accordingly. Moreover, the crack at the bottom right corner of the window (d), which is related to the mechanism that causes crack a, does mimic the behaviour seen in Figure 9a. Finally, for the crack at the top right corner of the window (b), no influence of the pre-damage is evident.

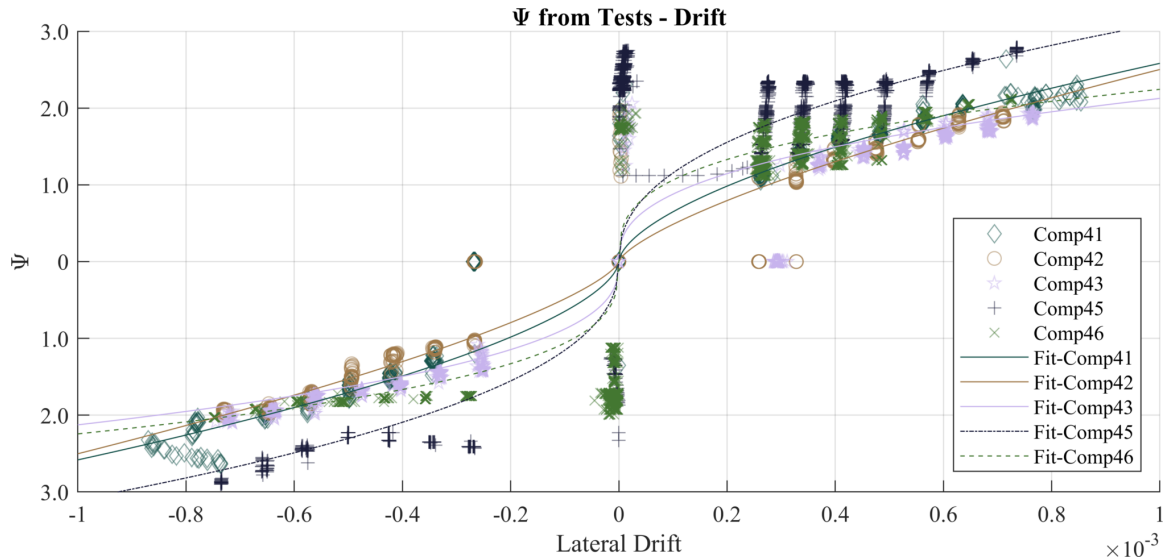


Figure 7. Damage parameter  $\Psi$  against values of drift for five walls, two of which (Comp45 and Comp46) were pre-damaged.

In terms of force degradation, no significant differences can be observed between the virgin and the pre-damaged walls. In Figure 8, the strength degradation during the multiple cycles only reveals that towards the end of the test, the pre-damaged walls do not display much degradation whereas the virgin walls (in particular Comp42) do show a decline in force.

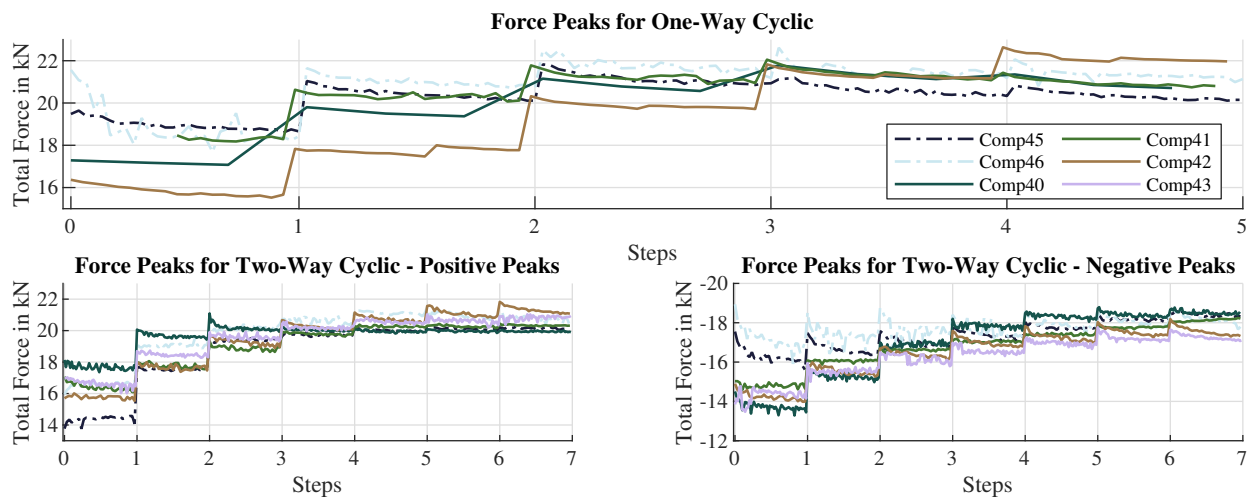


Figure 8. Comparison of force degradation during the tests.

Figure 9 compares the crack width during the two-way cyclic portion of the tests. This means that all the walls had been partly pre-damaged during the repetitive portion of the test; hence, Figure 10 looks at the one-way cyclic portion of the test. Here, only two cracks are compared as the other window corners are not engaged in the positive drift direction (see Figure 4f). In this figure, both pre-damaged cases develop cracks earlier than the virgin walls. Moreover, the width of crack “a”, a pre-damaged crack, is noticeably higher in the case of the pre-damaged walls, even before the pier detachment of Comp45 takes place.

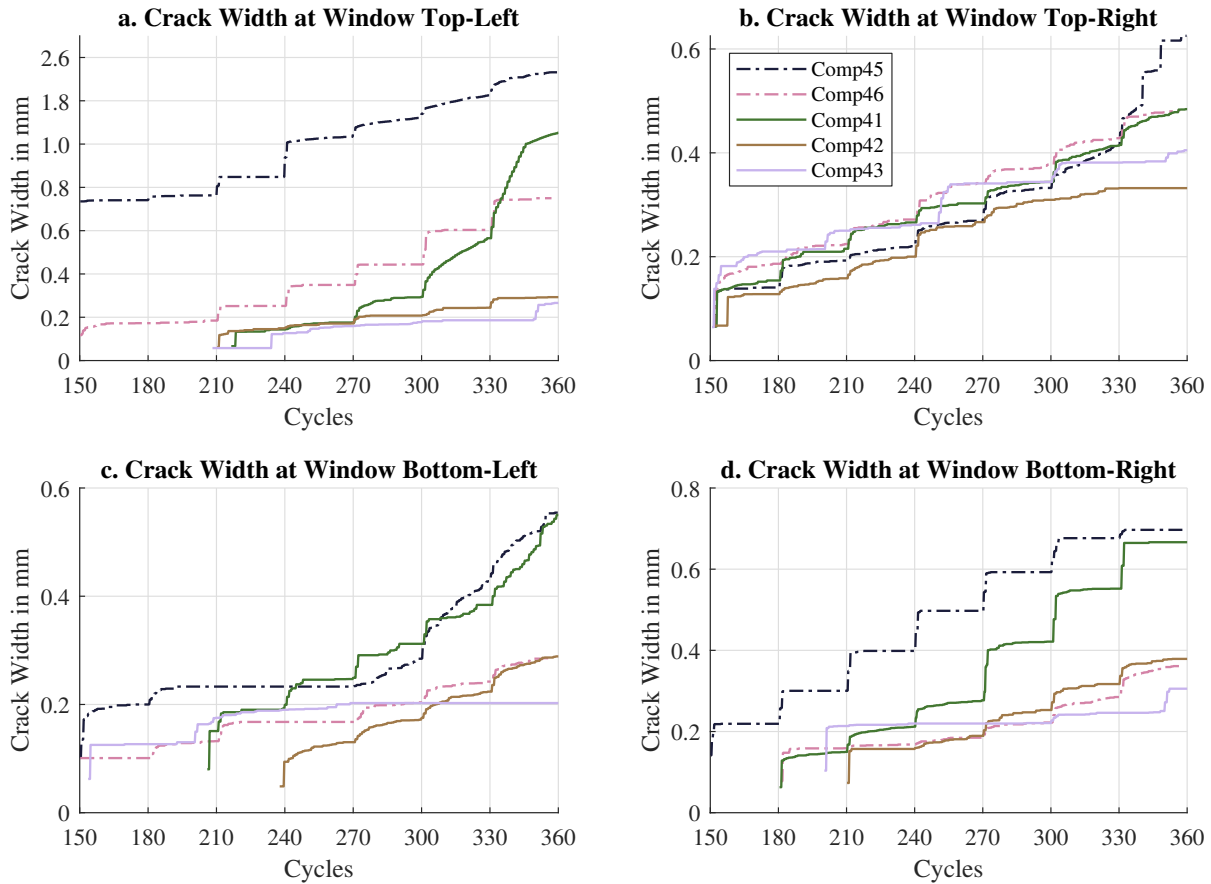


Figure 9. Comparison of crack width as detected by DIC for the two pre-damaged walls (Comp45 and Comp46) and the non-pre-damaged walls, for the four corners of the window during the two-way cyclic portion of the test.

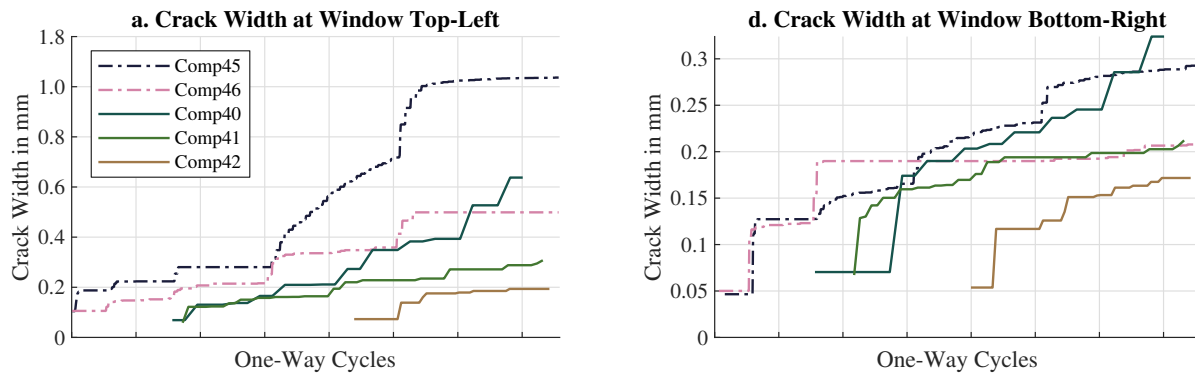


Figure 10. Comparison of crack width as detected by DIC for the two pre-damaged walls (Comp45 and Comp46) and the non-pre-damaged walls, for the two corners of the window during the one-way cyclic portion of the tests.

## 5. CALIBRATION AND COMPARISONS WITH COMPUTATIONAL MODELS

In this section, the two pre-damaged walls previously described are investigated with computational finite-element models. The models are validated and calibrated based on the experimental results from the two pre-damaged walls: TUD-Comp 45 and TUD-Comp 46. Material properties of the model are taken from companion tests on small specimens as part of the same experimental campaign (compression wallets, shear triplets, and in-plane bending tests). The walls are modelled with the software DIANA Finite Element Analysis, version 10.2. The non pre-damage walls (virgin walls) were tested and calibrated in a previous part of the study about which the reader is referred to Korswagen et al. (2019); the main distinctions are highlighted in this text.

In the first part of this section (5.1), the model of a pre-damaged wall is described and compared against the experimental results. Also, a comparison against the virgin wall is included. Then, in section 5.2, Non-Linear Time History Analyses (NLTHAs) of the validated model, with which realistic seismic excitations can be included, are presented and discussed. These analyses also compare different initial conditions and pre-damage configurations.

### 5.1 Calibration and Validation of the Pre-damaged Wall

The pre-damaged, in-plane loaded, baked-clay, brick masonry wall with an asymmetric window is modelled with 2D plane stress elements. The wall is 3050mm wide and 2700mm high with a thickness of 100mm. The opening is 800x1500mm and is placed 550mm from the bottom edge and 900mm from the left edge. The concrete beam above the window opening is modelled with a dimension of 1000x50mm. Both wall and lintel are modelled using 8-noded quadratic elements with a mesh size of 50x50mm. The integration scheme is set to 3x3 points per element. The top and bottom steel beams of the set-up are also modelled. One-dimensional beam elements having 3-nodes are employed. The two lines are placed at the top and bottom edge of the wall; as cross-section, HEB-600 and HEB-300 geometries are assigned, respectively. The top boundary condition is cantilever, thus allowing the top of the wall to rotate and displace vertically. Hence, only the bottom beam base is constrained in both horizontal and vertical directions. Before applying the in-plane top displacement to the wall, a vertical uniform load is applied as a line load on the top wall edge to simulate the 0.12MPa overburden. The mesh view of the DIANA model is shown in Figure 11.

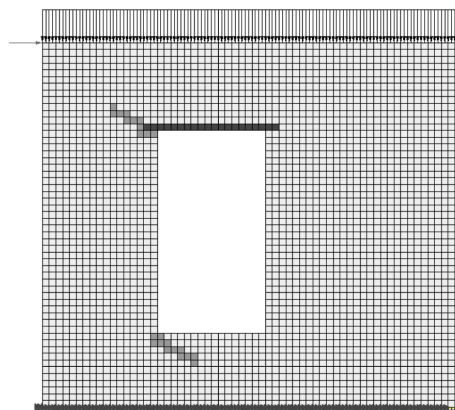


Figure 11. Finite Element Model of TUD-Comp 45 and 46 with 'weakened' elements.

Concrete and steel materials (for lintel and beams respectively) are modelled as linear elastic ( $\rho=2.4 \text{ ton/m}^3$ ,  $E=31\text{GPa}$ ,  $\nu=0.2$ ;  $\rho=7.85 \text{ ton/m}^3$ ,  $E=210\text{GPa}$ ,  $\nu=0.3$ ). Furthermore, to model the reduction in bond of the joints of the two specimens (see Figure 2), weak spots resembling the pre-damage are modelled (dark

grey elements in Figure 11). For these elements, half of the wall elastic properties are used. Moreover, no tensile strength is assigned to the material, since the plastic strips replicate an open crack. A shear resistance that accounts for the brick-PVC interaction is assigned to the weak spots (see Table 2). Accordingly, a non-linear material model is employed for both damage and non-damaged clay masonry. This allows to study the phenomenon of cracking in detail. As constitutive model, the Engineering Masonry Model with the diagonal stair-case option is used. This material model considers the orthotropic behaviour of the masonry, non-linearities in tension, shear and compression, and specific, different unloading/reloading characteristics according to experimental observations. Detailed information about the material model can be found in Schreppers et al. (2017) and Rots et al. (2016). The properties of clay masonry are partly taken from small companion tests and partly calibrated from the in-plane wall experiment results. A summary of the properties for both virgin and pre-damaged material is shown in Table 2. Physical non-linearities are considered in the model. A quasi-Newton (secant) approach is selected as iteration method. Either a force norm, with a tolerance of  $10^{-2}$ , or an energy norm, with a tolerance of  $10^{-4}$ , need to be satisfied for the equilibrium calculation. The Parallel Direct Sparse method is used to solve the system of equations. A tolerance of  $10^{-8}$  is here for employed.

Table 2. Material properties of virgin clay masonry and pre-damaged clay masonry. (1-Tested Value, 2-Estimated Value, 3-Computed Value).

<b>Material Properties for Clay Masonry</b>	<b>Virgin</b>		<b>Pre-damaged</b>	
<b>Density</b>	1 710 kg/m <sup>3</sup>	2	1 710 kg/m <sup>3</sup>	2
<b>Young's modulus perpendicular to bed-joints</b>	3 590 MPa	1	1 800 MPa	2
<b>Young's modulus parallel to bed-joints</b>	1 800 MPa	2	900 MPa	2
<b>Shear modulus</b>	1 620 MPa	2	800 MPa	2
<b>Tensile strength perpendicular to bed-joints</b>	0.15 MPa	2	0 MPa	2
<b>Fracture energy in tension</b>	10.8 N/m	3	Brittle	3
<b>Compressive strength</b>	12.2 MPa	1	12.2 MPa	1
<b>Compressive fracture energy</b>	28 600 N/m	1	28 600 N/m	1
<b>Friction Angle</b>	0.66 rad	1	0.46 rad	2
<b>Cohesion</b>	0.15 MPa	2	0.015 MPa	2
<b>Fracture energy in shear</b>	490 N/m	2	-	
<b>Predefined angle for diagonal cracking</b>	0.5	3	0.5	3

Three load cases are applied: dead load, overburden, and in-plane displacement-controlled loading. The displacement protocol is the same as the one employed in the experiment (see Figure 3), albeit with a reduced number of cycles per step, since the material model does not include force degradation for one-way cyclic loading; therefore, only one repetition per step is applied. Efforts to include strength degradation in the composite material model are underway, see Bindiganavile (2018).

When modelling the wall, strains focus at the foreseen crack locations and reveal the intended crack path during positive drift. This is illustrated in Figure 12a where the strain tensors are drawn. The final cracks comprising the crack location, width and length of the pattern produced by the FEM are depicted in Figure 12. As for the experimental results, cracks are evaluated from and to a cutoff width of 0.1mm and span a minimum length of 100mm. After the one-way cyclic protocol (Figure 12.b) three main cracks are detected: a rocking crack starting from the left edge at the height of the window, the opening of the pre-damage wall part at the top left corner of the window, and another rocking crack at the bottom right

corner of the window. At the end of the protocol (Figure 12.c), a rocking crack in the bed joints located in the larger pier at the top (right) window corner also occurs. These cracks are similar to those of the experimental test (Figure 6) differing only by the more pronounced stair-case trajectory of the test against the straighter one of the model, illustrated best by the crack at the top right corner of the window.

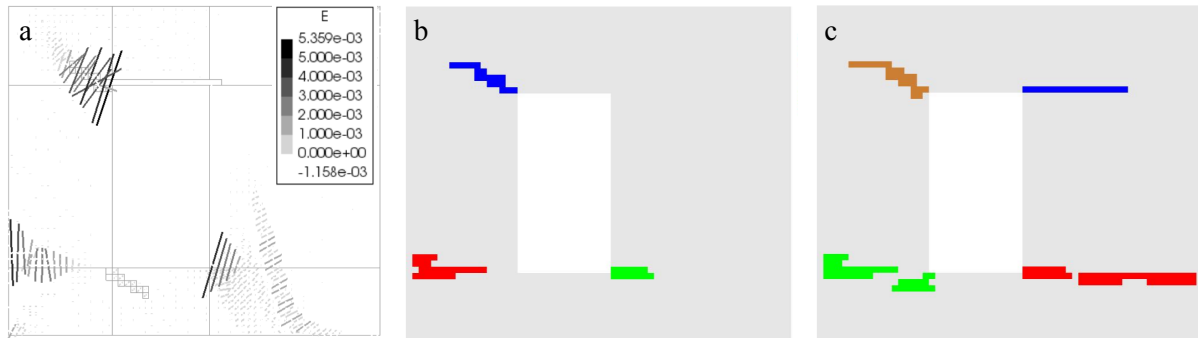


Figure 12. Left (a) Tensor plot of positive principal strain for a drift value of approximately to 0.4%. Right, Crack pattern of the FEM wall model (b) after the one-way cyclic and (c) at the end of the protocol.

Next, when plotting the force-drift behaviour (Figure 13), the model looks to be in reasonable agreement with the experiments. Both initial stiffness and positive force are well matched by the model, though the energy dissipation is overestimated in the two last cycles of the positive side. Regarding the negative side of the plots, the force (viewed as absolute value) and the energy dissipation are slightly higher when compared to the wall TUD-Comp 46. For the other specimen (TUD-Comp 45) the experimental hysteretic behaviour is comparable with the FE model.

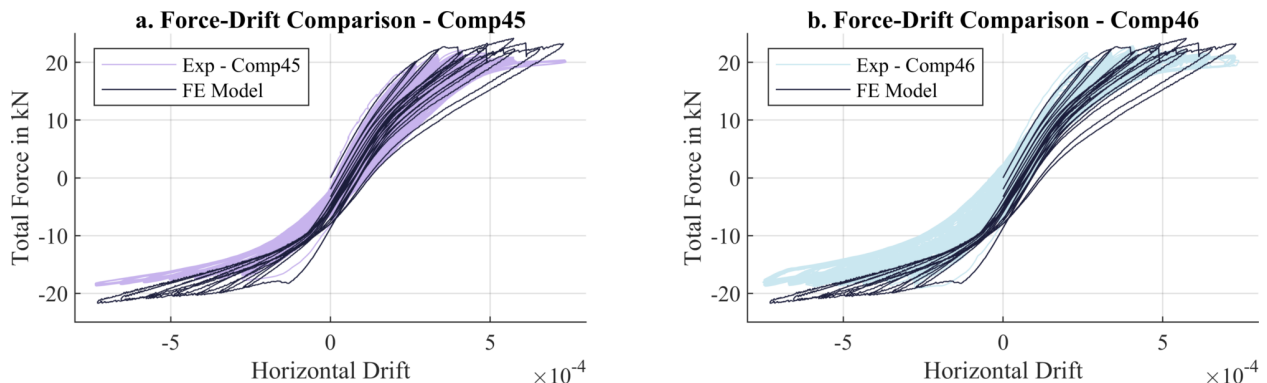


Figure 13. Force-Drift plots comparing the finite element model and the experimental (a) TUD-Comp 45 and (b) TUD-Comp 46 tests.

Furthermore, the finite element model calibrated only against the virgin walls (as discussed in Korswagen et al., 2019) does not differ significantly from the improved model (Figure 14). The difference between these two models can be found mainly in the modelling of the boundaries and in the material parameters. In the virgin walls only the top stiff beam was modelled using plane stress quadratic elements. A dummy stiffness and cross section was adopted for these elements. In the updated FE model, line beam elements are used to reproduce the rigid beams of the experiment (see Figure 1). Realistic values of stiffness, cross section and eccentricity are given to both bottom and top beam elements. In addition, the converge norm is switched from force or displacement (virgin wall) to force or energy (pre-damaged wall) since the analysis is run under displacement control. From these adjustments, the analysis duration and stability are improved. Ultimately, the material properties of the pre-damaged wall are updated based on the new small scale companion tests. Elastic, tensile and shear properties are slightly higher than the ones found in the

previous campaign (see Korswagen et al., 2019 for a collection of values). Hence, a minor increment in force and global stiffness is detected in the force-drift graph of Figure 14.

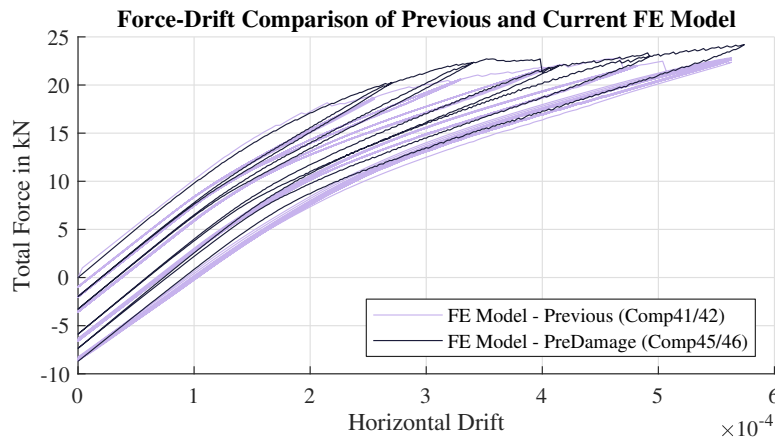


Figure 14. Force-Drift plots comparing the one-way cyclic part of finite element models: TUD-Comp 41/42 vs TUD-Comp 45/46.

## 5.2 Non-linear Time History Analyses

The calibrated model described in the previous section (5.1) is adopted for NLTHAs. The scope of the study is to compare the effect of specific initial conditions on the increase of the wall damage generated by a given earthquake excitation. Three different initial conditions are considered: no pre-damage, a virgin wall is considered; pre-damage via weak spots where the wall is weakened through weaker elements resulting in the same approach as in the previous section (5.1); and, pre-damage via settlement loading. For the latter, the wall is subjected to a settlement deflection case before applying the motion. The shape of such deformation, representing a right-side hogging settlement, is shown in Figure 15 (see also Figure 2).

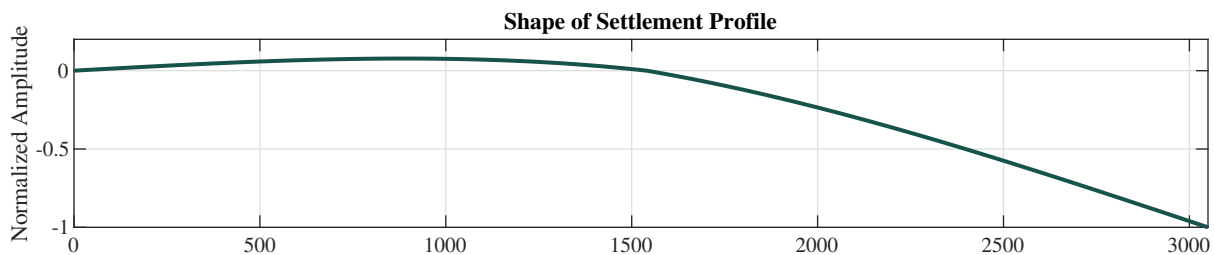


Figure 15. Settlement shape applied to the wall model.

The model for the NLTH analyses is slightly different in respect to the one used for quasi-static loading (section 5.1). Such adjustments include:

- Lateral reinforcements: two vertical linear beam elements, with a cross-section of one brick, are applied to the lateral edges of the wall. They simulate the constraints of two transversal walls in order to obtain realistic settlement damage.
- No steel beams: steel beams at the top and at the bottom edge of the model are removed.
- Mass element: a line mass element is applied at the top edge of the wall. A total mass of 8 tons, representing a fictitious slab and roof, acts during the dynamic motion without affecting the static condition.

- Non-linear boundary interface: an interface connects the bottom edge of the wall to the supports. The interface represents the local soil-structure interaction (see Van Staalduinen et al., 2018).
- Base acceleration: horizontal and vertical base motion is input as an acceleration at the base.
- Rayleigh damping (2%) based on the first two modes (participating mass) for the material model.

The material properties of concrete and clay masonry are the same of the calibrated model (Tables 2 and 3). The 6-node line interface at the bottom edge of the wall is characterised by no tension, with stiffness in compression equal to  $0.70 \text{ N/mm}^3$  and stiffness in shear equal to  $0.07 \text{ N/mm}^3$  (Giardina et al., 2015).

As input for the base motion, a set of horizontal and vertical components of the recent Zeerijp earthquake (8th of January of 2018) is chosen and applied at the base of the wall. This signal was recorded at the Garsthuizen station close to the epicentre and was selected mainly to be representative of a ‘near-field’ record of the ground motion in the Groningen region. The amplitude of the original signal is taken unmodified from its original peak ground acceleration (PGA) of  $0.11 \text{ g}$  in the maximum rotated horizontal direction and applied at the base of the model. This PGA is equivalent to a peak ground velocity (PGV) of approximately  $32 \text{ mm/s}$  for this record. Additionally, the effect of amplification factors with values of 2 and 3 are also investigated. These are arbitrary values selected to produce reasonable light damage within the interval defined as DS1. A representation of the set of records is given in Figure 16.

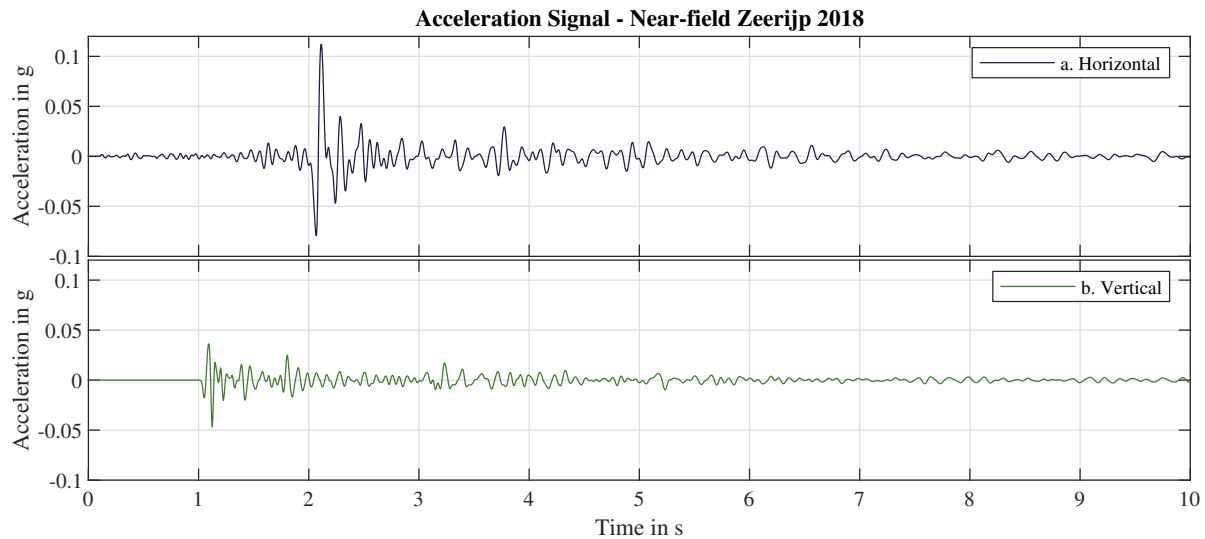


Figure 16. Near-field Zeerijp (2018 ) earthquake signal, (a) horizontal and (b) vertical acceleration plot.

The non-linear analysis procedure is subdivided in three phases. In the first phase, the gravitational load and an overburden of  $0.12 \text{ MPa}$  are applied. The second phase is used only for the case with pre-damage via settlement deflection. Here, the settlement shape, pictured in Figure 15, is assigned as displacement to the bottom side of the interface. The hogging deformation is applied at a rate of  $0.01 \text{ mm}$  per step, up to  $4 \text{ mm}$  of vertical displacement on the right edge of the wall. The third phase is related to the application of the dynamic motion. Horizontal and vertical accelerations are added to the bottom edge of the wall. The entire duration of the signal amounts to  $12.5 \text{ s}$  at steps of  $0.001 \text{ s}$  each.

Tensile and shear cracking values are extrapolated from the models. The damage situation is post-processed in the same way as DIC data for before and after the motion. For the latter, the maximum crack width experienced during the entire motion and the final residual damage are considered. The crack


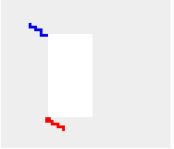
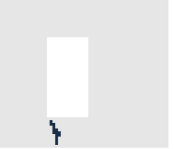
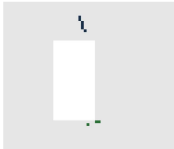
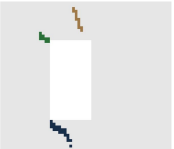
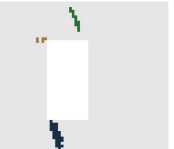

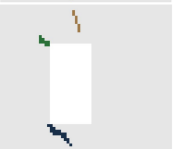
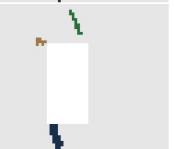
patterns and damage values are collected in Table 4, while Table 3 presents the  $\Psi$  values for the three seismic amplifications. Here one can observe that the virgin wall sustains noticeably less damage (40%) than the pre-damaged cases for the original earthquake PGA, but, as the PGA increases, the difference reduces (10-20%). Moreover, the damage increase ( $\Delta\Psi$ ) is considerably lower for the pre-damaged cases than for the virgin models. Similarly, doubling the PGA leads to a small damage increase (10-15%) for the pre-damaged cases, but to a 50% increase for the virgin walls. Between the two pre-damage methodologies, the inclusion of weak elements yields consistently higher damage, albeit not considerably so (15%). Furthermore, evaluating  $\Psi$  at the moment of maximum damage is akin to considering the residual state for all cases.

The damage patterns displayed in Table 4 reveal that the crack caused by settlement, whether by weakening of elements or pre-damaging of the model, is influential and becomes larger after the seismic motions. Accordingly, for the virgin walls, where such a crack was not present, it also does not appear. However, a crack on top of the window, absent from all cases before the motion, is triggered by the seismic excitation on all cases.

Table 3. Damage values for various ground motion PGA values with and without pre-damage.

$\Psi$	No Pre-damage			Pre-damage						
	Virgin walls			Weak elements			Settlement deflection			
	1x	2x	3x	1x	2x	3x	1x	2x	3x	
<b>Amplification of PGA</b>										
<b>Before</b>		0.0			1.1			1.5		
<b>Maximum of Motion</b>	1.2	1.8	1.9	2.0	2.2	2.4	1.9	1.9	2.1	
<b>Residual (after Motion)</b>	1.0	1.7	1.9	1.7	2.0	2.2	1.9	1.9	2.0	

Table 4. Crack pattern and damage value experienced before and after the motion phase, and residual damage at the end of the motion for different pre-damage conditions. All for no PGA amplification (1x0.11g).

Type	No pre-damage		Pre-damage			
			Weak elements		Settlement deflection	
<b>Damage before motion</b>		$\psi=0.0$		$\psi=1.1$		$\psi=1.5$
<b>Damage during Motion</b>		$\psi=1.2$		$\psi=2.0$		$\psi=1.9$
<b>Residual Damage</b>		$\psi=1.0$		$\psi=1.7$		$\psi=1.9$



## 6. CONCLUSIONS

The experimental tests conducted in this study, showed that full-scale, baked-clay brick masonry walls with a few weaker, pre-damaged joints are more susceptible to experiencing increased (light) damage when subjected to in-plane, lateral drift. This is particularly the case when the strains focus and follow the existing crack locations. Furthermore, non-linear time-history analyses calibrated upon these experiments and subjected to a representative seismic excitation, also show that models where pre-damage has been induced following a differential settlement case, are more prone to additional damage; incipient cracks ( $\Psi \approx 1$ ) caused by settlement actions are then enlarged by the seismic event becoming visible ( $\Psi > 1$ ) at peak ground velocities of approximately 30 mm/s, whereas models not subjected to settlement pre-damage, require stronger vibrations to display similar damage intensities. Nonetheless, peak velocities larger than 100 mm/s are necessary for the planar wall models to exceed the light damage state (DS1,  $\Psi > 3$ ).

## ACKNOWLEDGMENTS

This research was funded by Nederlandse Aardolie Maatschappij (NAM) under contract number UI67339 ‘Damage sensitivity of Groningen masonry building structures – Experimental and computational studies’, contract holders: Jan van Elk and Jeroen Uilenreef. This cooperation is gratefully acknowledged. The authors also express their gratitude to Piet van Staalduinen for linking this project to damage surveys; to Marianthi Sousamli for contributing to the calibration of the soil-structure interaction in the models; and, to Michele Palmieri from Arup for reviewing tasks.

## REFERENCES

- S. Bindiganavile Ramadas (2018). A Hyperbolic model for Degradation in Tension mode-I Fracture of Masonry: Implementation and Validation in Engineering masonry model. TU Delft Civil Engineering and Geosciences. November 2018. uuid:3c5dce16-f7c7-479f-80df-1bf141e0bf42
- M. Didier, G. Abbiati, F. Hefti, M. Broccardo, B. Stojadinovic (2018). Damage Quantification In Plastered Unreinforced Masonry Walls Using Digital Image Correlation. 10th Australasian Masonry Conference, 14-18 February, 2018
- G. Giardina, J.G. Rots, M.A.N. Hendriks (2013). Modelling of Settlement Induced Building Damage. TU Delft
- G. Giardina, M.A.N. Hendriks, J.G. Rots, (2015). Sensitivity study on tunneling induced damage to a masonry facade. *Engineering Structures* 89 (2015), 111-129
- F. Graziotti, U. Tomassetti, S. Kallioras, A. Penna, G. Magenes (2017). Shaking table test on a full scale URM cavity wall building. *Bulletin of Earthquake Engineering*, 15 (12), pp. 5329-5364
- S. Jafari, R. Esposito, J.G. Rots, F. Messali (2017). Characterizing the Material Properties of Dutch Unreinforced Masonry. *Procedia engineering*, 193, 250-257
- S. Jafari, R. Esposito (2019). Summary of material properties of existing Dutch masonry - updated URM abacus (version 2). Delft University of Technology. Report number C31B67WP1-16, version 02
- P.A. Korswagen, M. Longo, E. Meulman, C. Van Hoogdalem, (2017). Damage sensitivity of Groningen masonry structures – Experimental and computational studies. Report number C31B69WP0-11, Final report, version 1.1, 30th of December of 2017.
- P.A. Korswagen, E. Meulman, M. Longo, J.G. Rots (2018). Crack Initiation And Propagation In Unreinforced Masonry Structures Subjected To Repeated Load And Earthquake Vibration. 10th International Masonry Conference (IMC). 9-11 July, Milan, Italy.

- P.A. Korswagen, M. Longo, E. Meulman, J.G. Rots (2019). Crack Initiation And Propagation In Unreinforced Masonry Specimens Subjected To Repeated In-Plane Loading During Light Damage. Accepted for publication in Bulletin of Earthquake Engineering.
- F. Messali, G.J.P. Ravenshorst, R. Esposito, J.G. Rots (2017). Large-scale testing program for the seismic characterization of Dutch masonry walls. 16th World Conference on Earthquake, WCEE 2017, 9-13 Jan. 2017, Santiago, Chile.
- NAM (2016). Production, Subsidence, Induced Earthquakes and Seismic Hazard and Risk Assessment in the Groningen Field. NAM, Technical Addendum to the Winningsplan Groningen 2016. Downloadable from [www.NAM.nl](http://www.NAM.nl)
- J.G. Rots, F. Messali, R. Esposito, S. Jafari, V. Mariani (2016). Computational Modelling of Masonry with a view to Groningen induced Seismicity. 10th SAHC Structural Analysis of Historical Construction, Leuven
- G.M.A. Schreppers, A. Garofano, F. Messali, J.G. Rots (2016). DIANA validation report for masonry modelling. DIANA FEA report 2016-DIANA-R1601 TU Delft Structural Mechanics Report CM-2016-17, 143 pp
- P. Van Staaldin, K. Terwel, J.G. Rots (2018). Onderzoek naar de oorzaken van bouwkundige schade in Groningen Methodologie en case studies ter duiding van de oorzaken. Delft University of Technology. Report number CM-2018-01, 11 July 2018 - Downloadable from [www.NationaalCoördinatorGroningen.nl](http://www.NationaalCoördinatorGroningen.nl)
- I. de Vent, J.G. Rots, R.P.J. van Hees (2011). Structural Damage in Masonry - Developing diagnostic decision support. TU Delft.